AIAA SciTech Forum
8-12 January 2024, Orlando, FL
AIAA SCITECH 2024 Forum

10.2514/6.2024-1027

Optical Effects of a Temperature-Mismatched and Species-Mismatched Supersonic Mixing Layer

Aaron Fassler*, Sergey Leonov† and Stanislav Gordeyev‡
University of Notre Dame, Notre Dame, IN 46556

The aero-optical distortions caused by supersonic mixing layers over an optical window are relevant to the performance of hypersonic vehicles. Such mixing layers are typically temperature-mismatched and gas species-mismatched due to a need to cool the optical window. To investigate the effect of the mismatched properties across the mixing layer created by blowing a cool gas over a flat window, optical measurements of an $M = 2$ freestream air flow with a cooling two-dimensional gas jet were taken using Shack-Hartmann WFS and Schlieren photography techniques. The cooling jet gas properties were air at $M \approx 0.54$ and helium at $M \approx 0.30$. Total temperature of the freestream flow was varied from $295K$ to $750K$, while the total temperature of the cooling jet was kept constant at $295K$. Parameters of the mixing flow were examined using optical velocity methods. Two new scaling methods are examined. One scaling method assumes that the large vortical structures with related pressure drops are responsible for optical distortions. The second method is based on a pure mixing mechanism. It was demonstrated that distortions for air-air case were mostly pressure-dominant, while helium-air case was predominantly mixing-dominant.

I. Introduction

Hypersonic vehicles are becoming essential to the security of the United States and its partner nations. Critical missions include reconnaissance vehicles for gathering information anywhere in the world at short notice; high-speed, maneuverable missile-defense interceptors; hyper-velocity projectiles; and Conventional Prompt Strike weapons. Hypersonic flows around these vehicles are characterized by high stagnation temperatures, strong shock waves, and boundary layers with large temperature and density gradients. Many engineering and scientific challenges, such as reducing drag, mitigating thermal loads, advances in ramjet and scramjets, etc., have to be overcome for reliable hypersonic vehicles to become a reality. Of equal importance, hypersonic reconnaissance vehicles and interceptors require integrated optical sensors. Understanding the effects of both supersonic and hypersonic flows on the optical sensor performance, the so-called aero-optical effects, is a crucial requirement for such systems.

To successfully track a target, hypersonic vehicles typically use IR imaging cameras, usually behind a flat window mounted near the front of the vehicle, as shown in Fig. 1(a). The vehicle may also have side windows to send and receive data via laser beams as part of a high-speed and secure communication system. Since hypersonic flows significantly heat the vehicle surface, these windows need proper thermal protection. This is often achieved by blowing a coolant gas, such as nitrogen or helium, over the window to displace the hot air away from it [1–4]. While this approach does provide the needed window cooling, the mismatch in the velocity and density along the interface between the coolant gas and the ambient air forms a mixing shear layer over the window which introduces extra wavefront disturbances, as shown in Fig. 1(a).

Density variations due to vortical structures formed inside the mixing layer, mixing of gases with different densities, and the bow shock result in significant aero-optical distortions on an outgoing laser beam or incoming light. The aero-optical distortions, denoted as the Optical Path Difference (OPD), are proportional to the integral of the fluctuating density field,

$$OPD(x,z,t) = K_{GD} \int \rho'(x,y,z,t)dy \,, \tag{1}$$

where K_{GD} is the Gladstone-Dale constant, and the integration is performed in the beam propagation direction [5, 6]. Typically, the level of the aero-optical distortions is quantified by the time-averaged spatial root-mean-square of the

*Graduate Research Assistant, Aerospace and Mechanical Engineering Department. AIAA Student member.
†Research Professor, Aerospace and Mechanical Engineering Department. AIAA Associate Fellow.
‡Associate Professor, Aerospace and Mechanical Engineering Department. AIAA Associate Fellow.

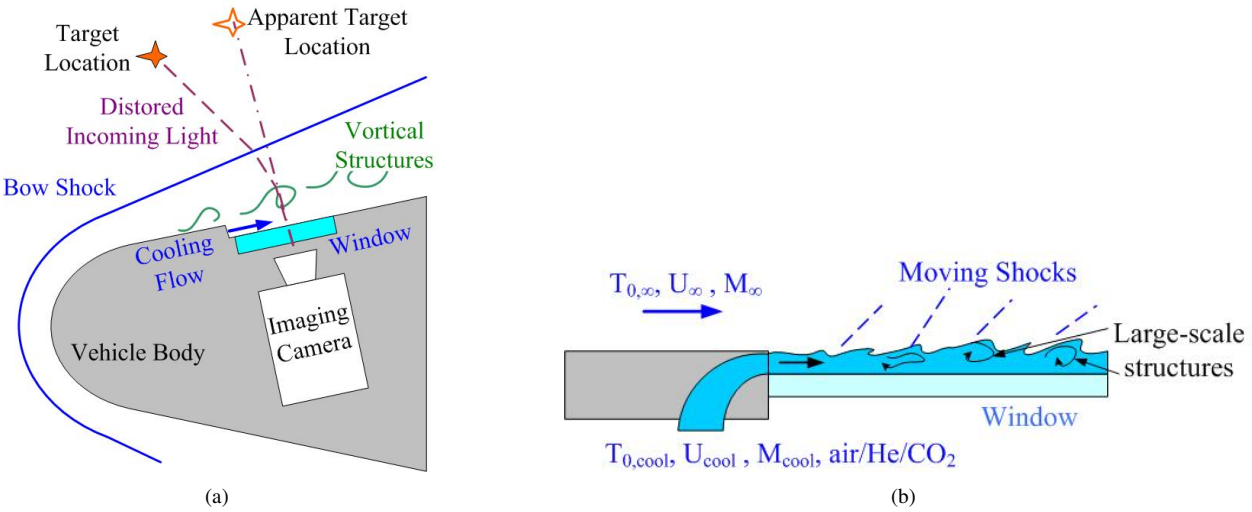

Fig. 1 (a) Aero-optical environment around a seeker window with a cooling flow in hypersonic flow, and associated image distortion. (b) Parameters of the mixing layer.

OPD-field,

$$OPD_{rms} = \overline{\langle [OPD(x,z,t)]^2 \rangle_{x,z}}\ , \tag{2}$$

where the angular brackets denote spatial averaging over the beam aperture and the overbar denotes time-averaging. The destructive interference of the distorted laser beam at the target results in a significant reduction of the laser intensity on a distant target [5, 6], and unsteady aero-optical distortions deteriorate visual representations of the target [4, 6, 7]. In addition, unsteady aero-optical distortions will result in an overall change in direction of the incoming or outgoing beam, called a boresight error (BSE), as shown in Fig. 1(a).

In real-world applications, a cooler gas is blown over the window to displace and prevent the hotter freestream gas from reaching the window, thus keeping the window temperature within a pre-determined range. The amount of cooling depends on the velocity, U_{cool}, static pressure, P_{cool}, and stagnation temperature, $T_{0,cool}$, of the coolant gas, as well as the gas type, listed in Figure 1(b). On the one hand, high velocities, pressures, and cooler temperatures do certainly provide better cooling. On the other hand, the mismatch in velocity between the cooling gas and the freestream will enforce the inviscid inflection instability mechanism, resulting in the formation of large-scale shear-layer structures. Enhanced entrainment of hot freestream gas into the cooler region near the window will reduce the efficiency of the window cooling and, more importantly, create additional density gradients, and associated aero-optical distortions. A mismatch of the static pressure of the two streams will result in either an over- or an under-expanded cooling jet. Deformations of the interface between the cooling jet and the freestream, such as those resulting from shear-layer structures due to inflection point instability, will lead to the formation of a series of shock and expansion fans over the window. Density gradients associated with these shocks and expansion fans will create additional aero-optical distortions. Finally, if the relative velocity difference along the coolant gas interface is larger than the local speed of sound, traveling shocks and expansion fans will be created at the interface, causing additional optical distortions.

The modeling is critical for both predicting and mitigating aero-optical distortions. A physics-based weakly-compressible model for the aero-optical effects of a subsonic two-dimensional shear layer was developed by Fitzgerald and Jumper [6, 8]. Assuming that the total temperature is the same on both sides of the shear layer, the model predicts that

$$OPD_{rms} \sim K_{GD}\rho_\infty M_c^2 \Lambda, \tag{3}$$

where Λ is a characteristic shear layer length scale along the beam propagation direction. The convective Mach number, M_C, is defined as [9]

$$M_C = \frac{U_1 - U_2}{a_1 + a_2}, \tag{4}$$

where U_1, a_1, and U_2, a_2 are the velocities and the speeds of sound, defined on the high- and the low-speed sides of the shear layer, respectively. It demonstrated that the model correctly predicts experimentally-observed levels of

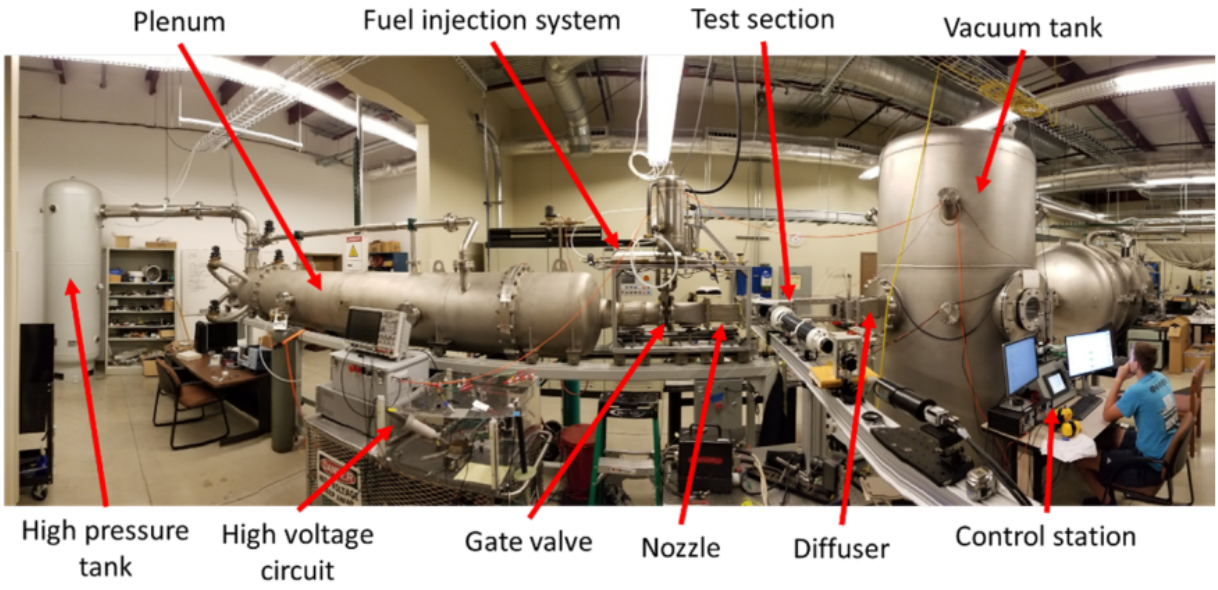

Fig. 2 View of SBR-50 facility with components labeled [16].

aero-optical distortions of subsonic and transonic shear layers [6, 10].

Unfortunately, this model does not take into account a mixing of two different gases. Also, the total temperature of both mixing streams is assumed to be constant, which is not the case for the cooling mixing flows. Finally, the model works for subsonic and transonic speeds only. So, there is a need to extend this model to supersonic and hypersonic speeds for general temperature/species mismatched two-dimensional mixing layers.

Another example of compressible mixing flows is a turbulent boundary layer. As pressure variations inside the boundary layer are generally small, the density fluctuations and the resulting optical distortions are mostly due to the velocity-dependent adiabatic cooling and heating. Using this notion, a model for aero-optical distortions for canonical boundary layers was built and demonstrated to successfully predict experimentally-observed distortions up to freestream Mach number of 5 [11, 12]. The model was also extended to predict aero-optical performance of the boundary layers with cooled or heated walls [13]. Still, there is a need to extend this model to mixing flows with different gas species. Ultimately, a generic model, combining the pressure fluctuations and velocity-related temperature variations, is needed to predict optical distortions of a wide class supersonic and hypersonic mixing flows.

In order to quantify aero-optical effects caused by two-dimensional cooling mixing flows over the window at supersonic speeds, this paper presents preliminary results from a series of experiments over a generic but relevant flat cooled window inside a shallow cavity with a large length/depth ratio for a freestream Mach number of $M = 2$ for different mixing parameters, including total temperature ratios $T_{0,\infty}/T_{0,cool}$, velocity ratios U_∞/U_{cool}, and different cooling gas species, air and helium. This paper is a continuation of the initial experimental studies of the same mixing layer, presented in [14], with important improvements to increase the accuracy of the measurements. The experimental results were used to extract flow parameters, like the mixing layer thickness and the spreading rate, as well as the velocity profiles across the mixing layer. The results were also used to test different models, proposed in the paper. A companion paper [15] presents results of wall-modeled large-eddy simulation of this experiment.

II. Experimental Setup

All experiments were performed in Notre Dame's SBR-50 tunnel in White Field Laboratories, which may be described as being configured as a combination of blowdown and Ludwieg tube schemes. The tunnel is designed for either $M = 2$ or $M = 4$ flow. For these experiments, $M = 2$ flow was selected. The driver section can be pressurized to stagnation pressures between 1 and 4 bar. A stagnation pressure of $P_0 = 2.6\ bar = 2.6 \times 10^5 Pa$ was selected for all experiments. The driver section can also be heated to stagnation temperatures between 300K and 775K. Typical steady-state flow duration is 0.5-2 s [16]. An overview of the SBR-50 facility can be found in Fig. 2.

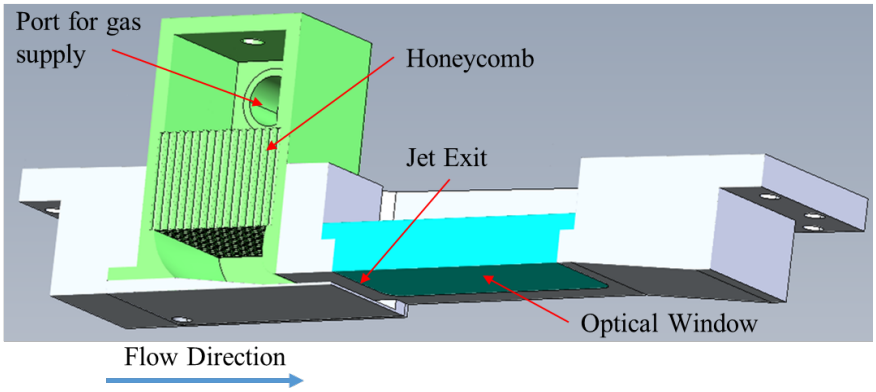

Fig. 3 Diagram of a test section insert with a vertical cross-cut with components and features labeled.

The test section insert, schematically shown in Fig. 3, is comprised of a larger aluminum frame, a 3-D printed plastic nozzle, and an aluminum cover plate with a thickness of 1 *mm*. These parts are secured to one another with screws. On the far upstream and far downstream edges, the test section insert conforms to the rest of the test section. In the center, the section is recessed. In addition, the test section insert contains an optical window set downstream of the nozzle exit. The depth of the step is 5 *mm* and the span of the insert is 76 *mm*, the same as the test section span. Just upstream of the step, the height of the test section is approximately 77 *mm*. The optical window is set directly downstream of the exit of the nozzle, and has a length of 100 *mm* and a width of 50 *mm*. The overall length of the cavity is 108 *mm*. The nozzle exit has a cross-sectional area of approximately 289 mm^2. Both spanwise faces of the nozzle contain 1/2 NPT threaded holes for gas supply from a compressed air tank. In all experiments, the gas supply comprised of air pressurized to 9 *psig* in order to match the static pressure between the exit jet in the freestream. In the midsection of the nozzle, a "honeycomb" mesh pattern is set in order to reduce turbulence from the gas supply. The nozzle section area is at a minimum at its exit, and therefore is designed to have an exit Mach number of 1. The upper face of the nozzle contains a 1/8 NPT threaded hole for a pressure probe to monitor the pressure of the gas supply.

For all tests, the gas supply was opened 500 ms after the tunnel flow startup. This is because after 500 ms, the tunnel flow is fully developed and tunnel conditions become mostly steady until approximately 1 s, as demostrated by the pressure trace in Fig. 4. For air as a cooling gas, later referred to as the air-air case, the gas supply was closed 1000 ms after the tunnel flow startup. In case of helium as a cooling gas, called the helium-air case, the gas supply was closed 750 ms after the tunnel flow startup, in order to conserve valuable test gas.

Stagnation temperature in the wind tunnel was first kept at ambient condition of 295K, then heated between 350K and 750K in steps of 100K. Tests with these conditions were repeated for both the air-air and the helium-air cases. A matrix of the test conditions can be found in Table 1.

Table 1 Test freestream conditions.

Run #	1	2	3	4	5	6
T_0	295 K	350 K	450 K	550 K	650 K	750 K
U_∞	510 m/s	560 m/s	630 m/s	700 m/s	760 m/s	820 m/s

A schematic of the optical measurements is presented in Fig. 5. As mentioned before, a large transparent flat optical window was flush-mounted into the floor of the cavity immediately downstream of the cooling jet nozzle. Another optical window of the same size was installed on the opposite (bottom) side of the tunnel test section to provide optical access in the wall-normal direction. A collimated laser beam 50 mm in diameter was forwarded into the test section in the wall-normal direction. The edge of the beam was placed 15 *mm* downstream from the nozzle exit plane. After being reflected from a flat return mirror outside of the test section, the beam was sent back to the optical table exactly along the same path it came into, thus doubling the optical signal. The outgoing beam was forwarded into a high-speed Shack-Hartmann wavefront sensor (WFS) to measure time-resolved spatial wavefronts caused by the turbulent flow in the cavity. The high-speed camera used in all tests was a Phantom v2512 camera. The lenslet array placed on the camera lens has a pitch of 0.3 *mm* and a focal length of 38.2 *mm*. Tests were performed at a sampling frequency of 75 kHz.

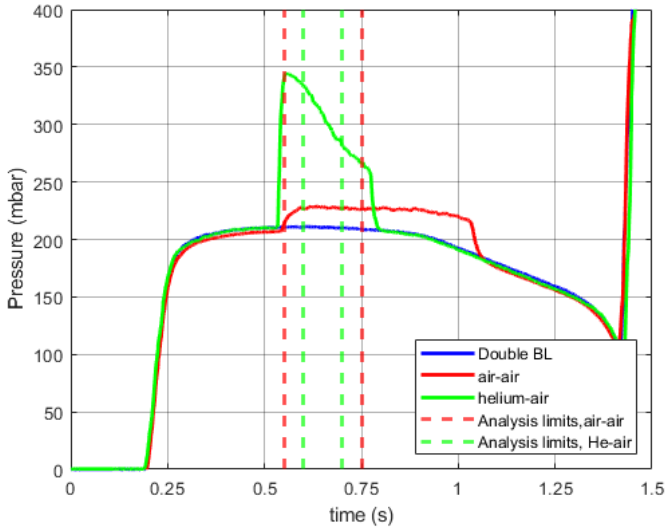

Fig. 4 Time-dependent static pressure values from a pressure probe set downstream of the test section. Vertical lines indicate the time intervals used for the wavefront analysis.

From this data, both deflection angles and wavefront data were obtained. A labelled picture of the Shack-Hartmann Wavefront Sensor setup is shown in Fig. 6.

To compliment the wall-normal optical measurements, a time-resolved Schlieren system in the spanwise-direction was used to qualitatively evaluate the flow topology of the incoming boundary layer and the mixing layer. Schlieren imaging was performed in the spanwise direction in order to qualitatively characterize the flow and to determine convective velocities via optical methods. The Schlieren setup consisted of an LED light source, two 5-inch diameter telescopes, and a vertical knife edge. A picture of the Schlieren setup is shown in Fig. 7.

The spatial resolution of the Schlieren setup was 8,800 pixels/m. A representative frame of the Schlieren image with the cooling nozzle flow on is shown in Fig. 8. An incoming turbulent boundary, a boundary layer on the opposite wall, and the resulting mixing layer over the cavity can be clearly seen. A weak oblique shock is also formed at the corner of the step.

It is apparent that the boundary layer on the wall opposite the mixing layer is a potential contaminating effect on the wall-normal optical measurements. Previous analysis used a model for canonical boundary layers to determine the level of additional distortion caused [14]. However, it is valuable to determine this quantity experimentally as well. In order to quantify and remove the aero-optical effects of the boundary layer on the opposite wall, additional Shack-Hartmann WFS measurements were taken, where the cooling jet test section insert was removed and replaced with an insert identical to the opposite insert. In this case, the laser beam propagated through two statistically-independent boundary layers on both sides of the test section. Later these tests will be refer to as the boundary layer measurements. Wavefront measurements were taken at the same 6 experimental stagnation temperatures, presented in Table 1, and the related aero-optical distortions due to the single boundary layer were calculated, as described in the next section.

III. Data Reduction Approaches

A. Optical Velocity

In order to temporally resolve the moving structures at speeds close to the freestream speed, the Schlieren image size was reduced to a resolution of 768x256 pixels, as shown in Fig. 9, enabling a higher recording rate of 100 kHz. Several areas of interest in the Schlieren images were identified, as shown in Fig. 9. Box A, with a size of 70x100 pixels, is located in the incoming boundary layer. Box B, with a size of 30x100 pixels, was placed at the exit of the cooling jet. Box C, with a size of 120x200 pixels, was positioned at the center of the SHWFS aperture and encompasses the mixing layer in the wall-normal direction.

Using the data from each identified box, spatio-temporal Fourier transform was performed on the mean-removed

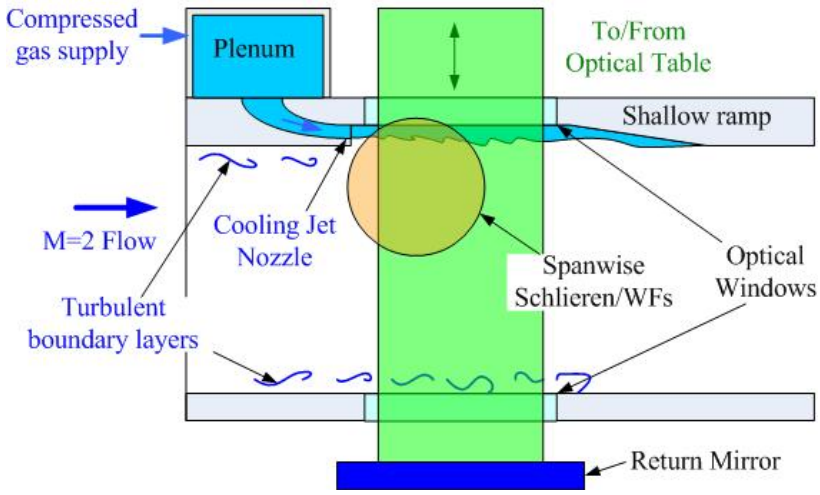

Fig. 5 Schematic of optical measurements.

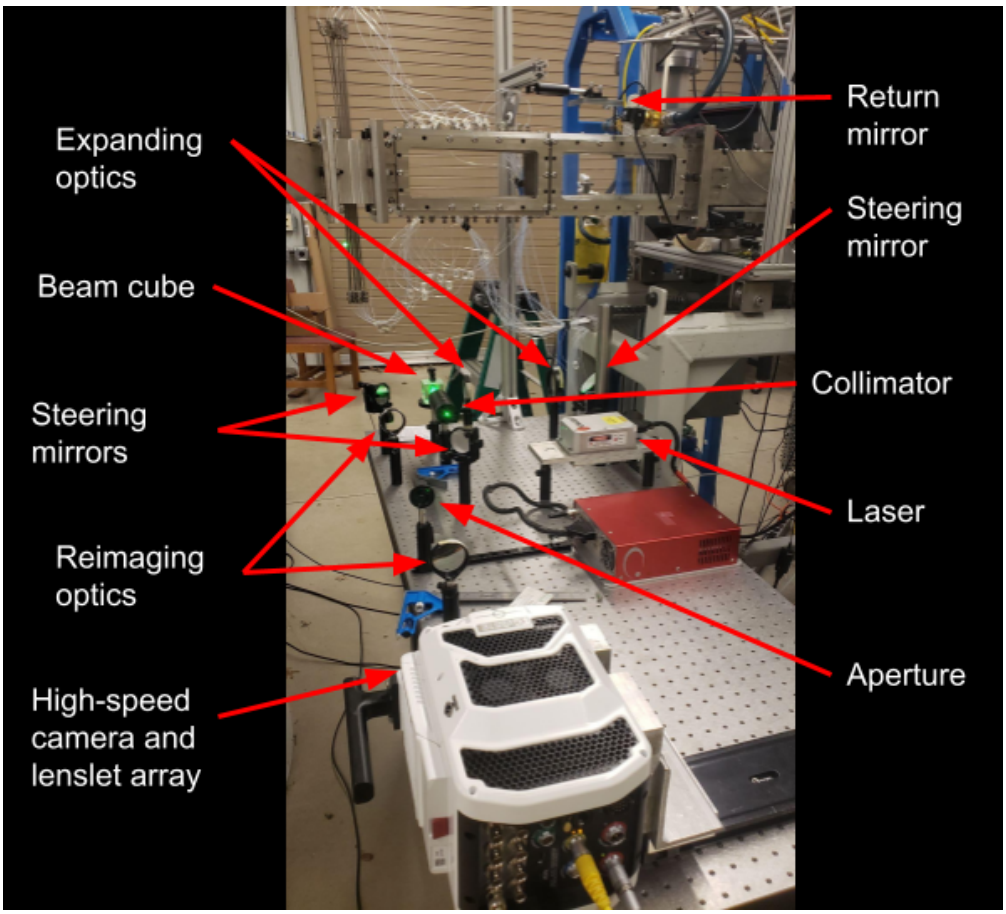

Fig. 6 View of Shack-Hartmann WFS with components labeled.

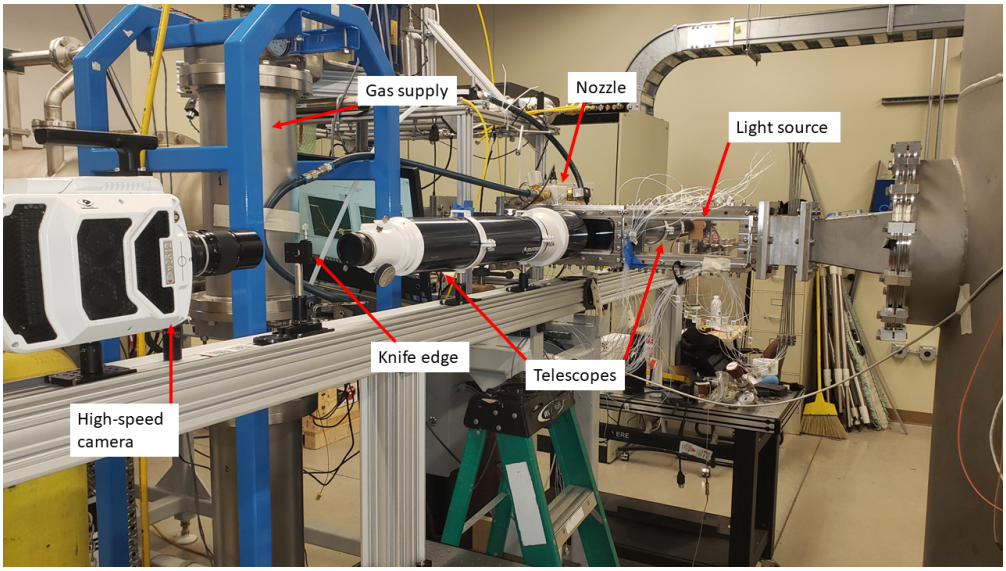

Fig. 7 View of Schlieren setup with components labeled.

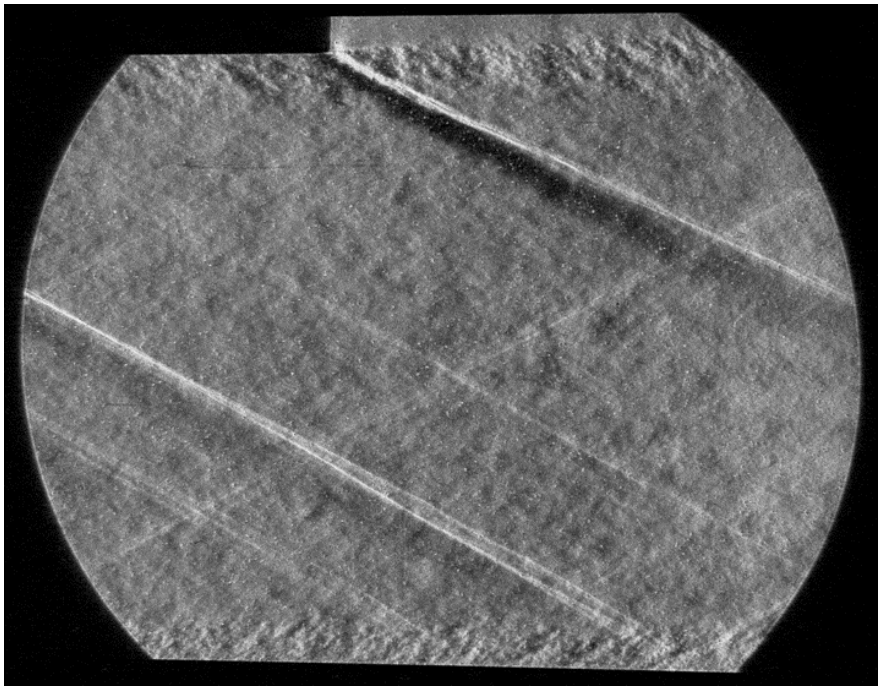

Fig. 8 Spanwise Schlieren image with nozzle flow on.

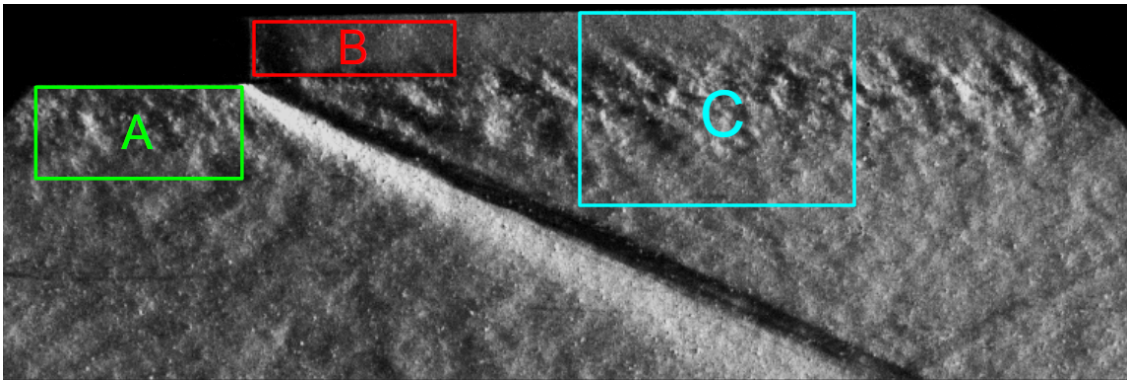

Fig. 9 Schlieren image with areas of interest highlighted in color boxes.

Schlieren image data at each wall-normal location. The number of spatial points used was dependent on the width of the area of interest. To reduce computing time, only the first 10,000 temporal points (with a total duration of 0.1 sec) after the nozzle flow was turned on were used. No windowing or block averaging was used in the analysis. The Fourier power spectrum, taken from the Schlieren data inside Box C, is shown in Fig 9. The convective nature of the aero-optical distortions is manifested as a diagonal branch, identified by solid circles. The slope of this branch, obtained by performing a linear fit (indicated by a dashed line), is equal to the inverse of the convective speed, U_c, of these convecting structures at this wall-normal location.

In addition to the main branch, many other branches are present in Fig. 10(a) above and below the main branch due to aliasing of the main branch in the frequency domain. To extend the frequency range in the main branch and to improve the accuracy of the convective velocity estimate, a stacking method [12, 17] was used. In the stacking method, copies of the 2-D spectrum, shifted by a multiple of the sampling frequency in both positive and negative frequency directions, are added to the original spectrum to reduce aliasing. The resulting extended spectrum is shown in Fig. 10(b). Note that the original 2-D spectrum has been stacked once on either side in the temporal frequency space. The resulting spectrum shows a well-defined "branch" in both spatial and temporal frequency, with more points in the frequency range. The extended convective branch is identified by computing local weighed maxima, indicated by solid red circles. For every extended spectrum at a given wall-normal location, the linear fit was used to calculate the convective speed at this location.

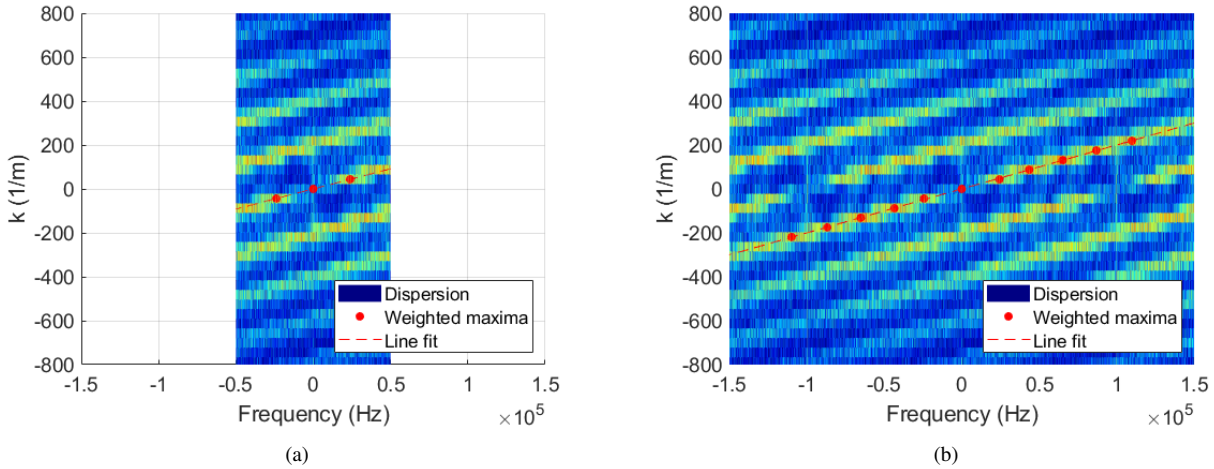

Fig. 10 2-D Fourier transforms of a horizontal section of Schlieren data with convective velocity line fit overlaid, (a) without stacking (b) with stacking.

B. Aero-optical distortion levels

The Shack-Hartmann sensor measured deflection angles (θ_x, θ_z) at discrete locations (x, z) over the aperture. The deflection angles are related to the wavefront, $OPD(x, z, t)$, via the spatial gradient,$\theta_x = \partial OPD/\partial x, \theta_z = \partial OPD/\partial z$. In-house software was used to numerically integrate the measured deflection angles to obtain the wavefront time sequences over the aperture using Southwell's method [18]. To make the solution unique, the spatial mean value of the wavefront (piston component) was forced to zero at every time, $\int OPD(x, z, t)dxdz = 0$. In addition, the time-averaged wavefront (steady lensing) and instantaneous tip/tilt component were removed from each wavefront. Finally, the aperture-averaged levels of aero-optical distortion, OPD_{rms}, were calculated using Eq. 2 for different test conditions.

As noted before, the SHWFS laser bean must pass through both the mixing layer and the boundary layer on the opposite wall. Assuming the optical distortions from the contributing flows are statistically independent, the contributions to optical distortions may be described as [6]

$$OPD^2_{rms,total,ML-BL} = OPD^2_{rms,ML} + OPD^2_{rms,BL} \tag{5}$$

In case of the boundary layer measurements, where the laser beam passed through two boundary layers, aero-optical distortions from each boundary layer can be assumed to be the same. In this case, the levels of the aero-optical distortions from one boundary layer, $OPD_{rms,BL}$, can be computed from the total level of the distortions due to two boundary layers, $OPD_{rms,total,BL-BL}$, since

$$OPD^2_{rms,total,BL-BL} = OPD^2_{rms,BL1} + OPD^2_{rms,BL2} = 2 \cdot OPD^2_{rms,BL}$$

Therefore, to determine $OPD_{rms,ML}$ for the mixing layer alone,

$$OPD^2_{rms,ML} = OPD^2_{rms,total,ML-BL} - \frac{1}{2} OPD^2_{rms,total,BL-BL} \tag{6}$$

In addition, since the SHWFS aperture spans approximately the width of the test section, it will capture aero-optical effects from the side walls of the test section. To account for this, the spatial points comprising the area of the side-wall boundary layers were masked out before the wavefronts were calculated.

IV. Results

A. Boundary Layer Effects

The levels of aero-optical distortions due to the single boundary layer for different stagnation temperatures were computed, as discussed before, and presented in Figure 11 as blue circles. The overall levels were found to be between 0.04 and 0.045 microns. In the previous measurements of the mixing layer [14], the boundary layer on the tunnel wall was estimated to have a thickness of 5 mm. Using the model for the aero-optical distortions due to the canonical boundary layer [11], it is possible to estimate aero-optical effects of the canonical boundary layer. The results are also presented in Fig. 11 as red triangles. Experimental values were found to be significantly larger, suggesting a non-canonical BL in the test section. The reasons for the non-canonical nature of the boundary layer in the test section are currently under investigation.

In [14], the boundary layer was assumed to be a canonical one, and the theoretically-predicted levels of aero-optical distortions of were computed using the model and removed from the experimental data. As a result, the optical distortions, related to the mixing layer, were over-estimated. In this paper, measured $OPD_{rms,BL}$ due to the real boundary layer were removed from the overall optical data to provide more accurate values of the optical distortions due to the mixing layer only.

B. Speed and Temperature Estimates from Schlieren Data

From the analysis of convective velocities for Schlieren data, velocity profiles at the nozzle exit, the upstream boundary layer, and multiple downstream locations within the mixing layer were computed, as described before. Previous analysis of the region indicated as box A in Fig. 9 confirmed a boundary layer thickness of 5 - 6 mm [14]. Previous analysis produced freestream velocities and, assuming adiabatic flow, freestream temperatures, that agree well with a previous flow characterization study of the SBR-50 tunnel [14, 16].

The cooling nozzle exit velocities, extracted from the region indicated by box B in Fig. 9 and averaged over all

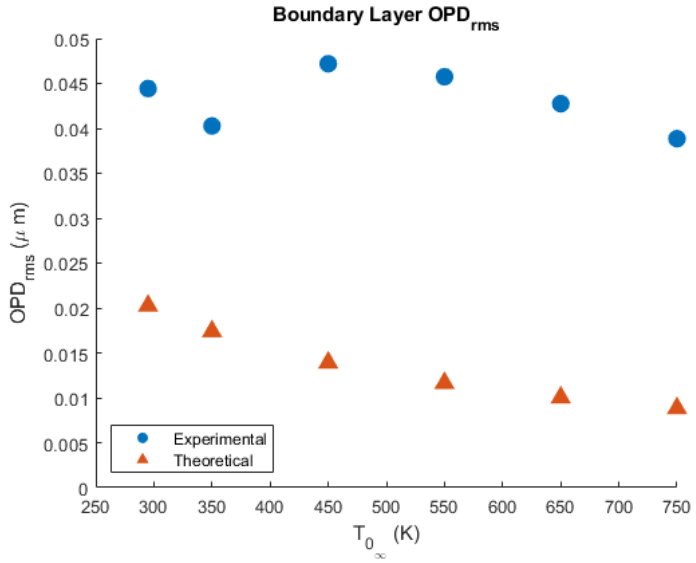

Fig. 11 Theoretical and experimental values of aero-optical distortions for a single boundary layer.

wall-normal locations, are shown in Fig. 12. It can be seen that the nozzle exit velocity is consistent across varied freestream total temperatures, as expected.

Using the values for cooling nozzle exit velocity, the Mach number of the nozzle flow can be calculated. Mach number is defined as

$$M = \frac{U}{a} = \frac{U}{\sqrt{\gamma RT}} \tag{7}$$

where U and T is the local values of the flow velocity and static temperature. The freestream temperature is dependent on local Mach number and therefore generally unknown. Assuming isentropic flow,

$$T = T_0 \left(1 + \frac{\gamma - 1}{2} M^2\right)^{-1},$$

substituting this equation into Eq. 7 and solving for M, we get the following equation,

$$M = \frac{U}{\sqrt{\gamma RT_0 - \frac{\gamma-1}{2} U^2}}. \tag{8}$$

Thus, if the stagnation temperature and the local speed are known, the corresponding local Mach number can be found using Eq. 8. Since for the cooling side of the mixing flow $T_{0,cool}$ is known to be 295K, it was determined that $M_{cool,air} = 0.54$ and $M_{cool,He} = 0.30$.

C. Mixing Layer Thickness

In order to quantify the thickness of the mixing layer at different downstream locations from the spanwise Schlieren data, the temporal standard deviation of the intensity values of the spanwise Schlieren data at each pixel was calculated. The results for the air-air and the helium-air cases for $T_0 = 295K$ are shown in Fig. 13. High intensity variation can be observed at the oblique shock originating from the edge of the step, the incoming boundary layer, and the mixing layer. For the helium-air case, Fig. 13(b), density fluctuations and related Schlieren intensity variations inside the mixing layer are significantly larger for the helium-air case due to mixing of different gases with very dissimilar densities. In comparison, densities on both sides of the mixing layer for the air-air case, Fig. 13(a), are similar, resulting in smaller mixing-related density variations.

Intensity variations at selected downstream locations, measured from the beginning of the mixing flow, are shown in Fig. 14. It can be seen that intensity variation is biased toward higher wall-normal locations, due to the presence of the

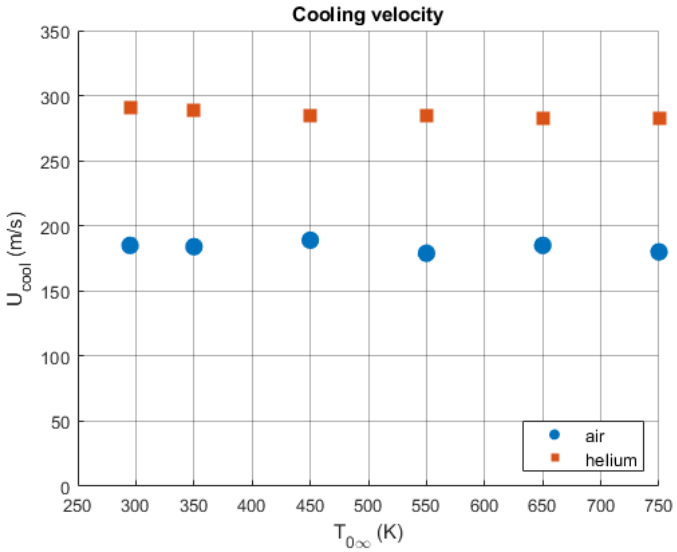

Fig. 12 Estimated cooling nozzle exit velocities as a function of freestream total temperatures for air and helium.

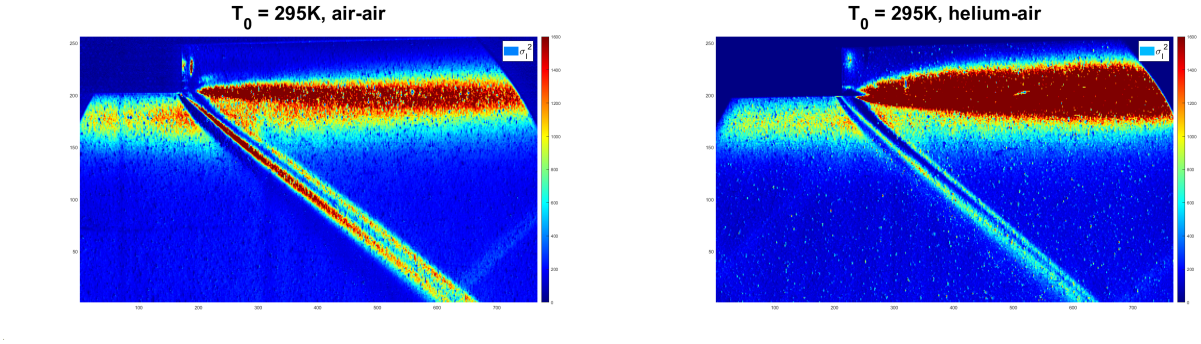

(a) (b)

Fig. 13 Temporal standard deviation of intensity, $T_0 = 295K$ for (a) air-air and (b) helium-air. Pixel numbers are plotted on axes.

oncoming boundary layer. To account for this, only the half of the peak closer to the wall was taken, then mirrored. After mirroring, the curve then becomes symmetric, and a Gaussian curve can be fitted to the intensity values, and the half-width of the curve calculated. This provides a metric for estimating the local mixing layer thickness, δ_{ML}, the results of which for different total temperatures are shown in Fig. 15. The thickness increases approximately in a linear fashion in the streamwise direction, as expected for mixing layers. The mixing layer becomes thinner at higher freestream temperatures above 500K. The reasons the mixing layer is abnormally thicker for the 450K air-air case, also observed in the initial studies [14], are not clear at this point and require further investigation. For modelling efforts, described later in the manuscript, an averaged value between the mixing layer thicknesses for T_0 = 350K and 550K was used to approximate the mixing layer thickness at $T_0 = 450K$.

Fig. 16 summarizes the spreading rate of the mixing layers, obtained from the slopes of the lines fit to the data in Figs. 15(a) and 15(b). For the air-air case, the spreading rate appears to decrease with increasing $T_{0\infty}$, then increase after the large spike in spreading rate at $T_{0\infty} = 450K$. For the helium-air case, the spreading rate appears to consistently decrease with increasing $T_{0\infty}$. In general, the spreading rate of the mixing layer was found to be larger for the helium-air case compared to the air-air case. One possible reason for this is the compressibility effects. Using Eq. 4 , the convective Mach numbers for the air-air case were computed to be between 0.55 and 0.85, while for the helium-air case, they are lower, between 0.12 and 0.26. It was observed that the mixing layers with larger convective Mach numbers generally have significantly smaller spreading rates than those with smaller subsonic convective Mach numbers [19].

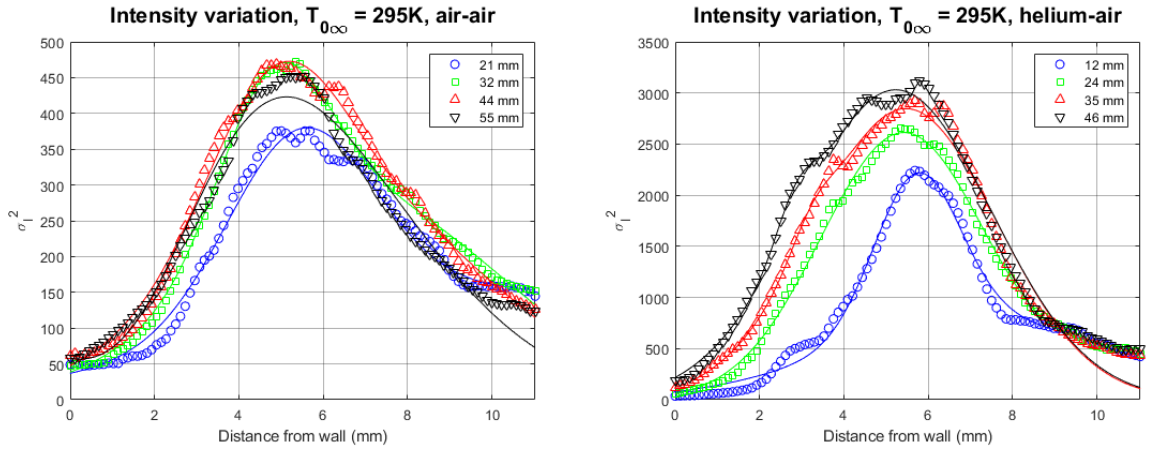

(a) (b)

Fig. 14 Temporal standard deviation of intensity at selected downstream locations for (a) air-air and (b) helium-air.

Figs. 17 and 18 show velocity profiles extracted from box C in Fig. 9. This data provides another method to quantify mixing layer thickness in a future analysis. Note that for the helium-air case, the normalized profile does not reach 0 at the wall. One possible reason for this is that density fluctuations are too low on the helium side. Another is that the mixing layer has spread nearly to the wall, causing extracted velocities to be higher in its vicinity.

D. Levels of Aero-Optical Distortions and Proposed Models

Relevant properties for the air-air and the helium-air cases are listed in Tables 2 and 3, respectively. As a reminder, the sub-indices "∞" and "$cool$" refer to the higher and lower velocity sides of the mixing layer, respectively.

Table 2 Flow properties, air-air.

$T_{0,\infty}$	295 K	350 K	450 K	550 K	650 K	750 K
$r = U_{cool}/U_\infty$	0.35	0.32	0.28	0.26	0.24	0.22
$s = \rho_{cool}/\rho_\infty$	0.59	0.70	0.90	1.1	1.3	1.5
U_c/U_∞	0.72	0.69	0.65	0.62	0.59	0.57
M_{cool}	0.54	0.54	0.54	0.54	0.54	0.54
$OPD_{rms,ML}$ (μm)	0.0286	0.0480	0.0372	0.0493	0.0490	0.0412

Table 3 Flow properties, helium-air.

$T_{0,\infty}$	295 K	350 K	450 K	550 K	650 K	750 K
$r = U_{cool}/U_\infty$	0.57	0.53	0.47	0.42	0.39	0.36
$s = \rho_{cool}/\rho_\infty$	0.078	0.093	0.12	0.15	0.17	0.20
U_c/U_∞	0.91	0.89	0.86	0.84	0.82	0.80
M_{cool}	0.30	0.30	0.30	0.30	0.30	0.30
$OPD_{rms,ML}$ (μm)	0.0606	0.0560	0.0580	0.0565	0.0504	0.0412

Here U_c is the isentropic approximation of the convective speed of the coherent structures in the mixing layer, which

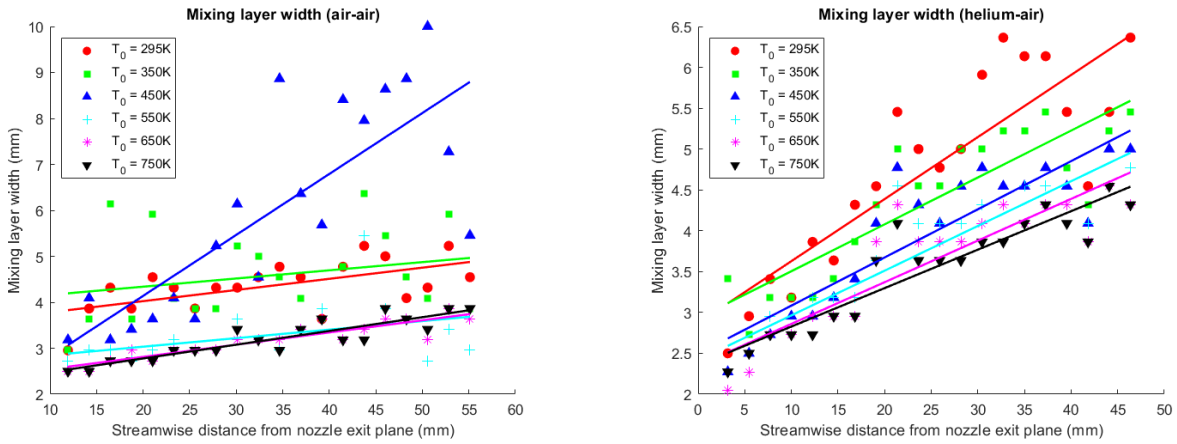

Fig. 15 Streamwise evolution of the mixing layer thicknesses, based on half-width of intensity variations at different total temperatures for (a) air-air and (b) helium-air.

can be estimated as [9]

$$U_c = \frac{U_\infty + U_{cool}\sqrt{\frac{\rho_{cool}}{\rho_\infty}}}{1+\sqrt{\frac{\rho_{cool}}{\rho_\infty}}}. \tag{9}$$

Note that Eq. 9 is also valid in case of dissimilar gases, when $\gamma_{cool} \neq \gamma_\infty$.

The collected wavefronts were processed, as discussed before, and the results are provided in Tables 2 and 3 as well. Since these values were computed by subtracting generally large optical distortions of the boundary layer on the opposite wall from the overall distortions, the uncertainty of the measurements will be somewhat high. However, the numerical simulations of the mixing layer for $T_{0,\infty} = 295K$ gave the value of the aero-optical distortions of 0.03804 μm [15], which is in between the observed experimental results of 0.0286 μm for 295K and 0.0480 μm for 350K.

1. Model: Air-Air Case

The obtained experimental results for different total temperatures versus the subsonic model, Eq. 3, are presented in Fig. 19(a); clearly the model does not work at supersonic speeds. This is expected, as it was mentioned in the Introduction, that the existing model fails to work at supersonic speeds and also assumes that the total temperatures are the same on both sides of the shear layer. Still, the the model correctly identified the main source of aero-optical distortions in the subsonic and transonic shear layers, which are regions of lower pressure, referred to as pressure "wells", inside the large-scale coherent vortical structures, convecting at the speed of U_C [8]. The pressure gradient of these "wells" balances the centripetal acceleration of the rotating flow. It is straightforward to derive [6] that the pressure drop, ΔP, inside the vortical structure is

$$\Delta P \sim \rho_{ref}(U_\infty - U_c)^2,$$

where ρ_{ref} is some reference density.

Assuming an isentropic flow, same gas on both sides, $\gamma_{cool} = \gamma_\infty = \gamma$, and small density/pressure variations, using the equation of state and the definition of Mach number, the density drop inside the vortical structure becomes

$$\frac{\Delta P}{P_\infty} = \gamma\frac{\Delta\rho}{\rho_{ref}} \sim \gamma\frac{\rho_{ref}(U_\infty - U_c)^2}{P_\infty} \sim \frac{(U_\infty - U_c)^2}{a_{ref}^2}. \tag{10}$$

Finally, using a bulk-flow approach [20], and assuming that the OPD_{rms} is proportional to the bulk density fluctuation levels, ρ_{rms}, and the characteristic thickness of the mixing layer along the beam propagation, Λ, we can get a new scaling for the aero-optical distortions of the supersonic mixing layers, dominated by the pressure "wells",

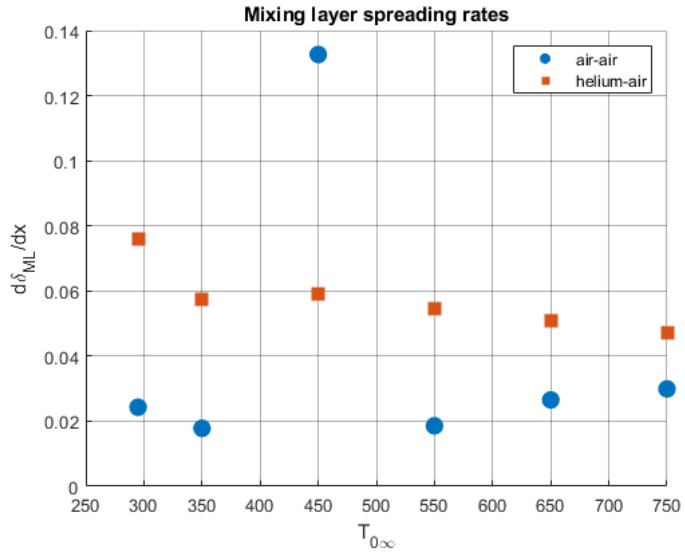

Fig. 16 Spreading rates at all total temperatures for both test gases.

$$OPD_{rms} \sim K_{GD}\Delta\rho\Lambda \sim K_{GD}\rho_{ref}\frac{(U_\infty - U_c)^2}{a_{ref}^2}\Lambda, \tag{11}$$

In these studies, a half-width of the mixing layer from Figure 15, averaged over the Shack-Hartmann WFS beam aperture were used, $\Lambda = \delta_{ML}$.

It is straightforward to show that if the freestream values of the density and the speed of sound are chosen as the reference quantities, Eq. 11 becomes Eq. 3 [6]. In general, for two-dimensional mixing flows in the frame of reference moving at the convective speed, a stagnation point occurs between two vortical structures [19]. A a consequence, all fluidic quantities, like density and temperature, must be continuous across the stagnation point. We have chosen reference values of the density and the speed of sound to be the corresponding values at the stagnation point. The reference stagnation temperature at the stagnation point can be assumed to be the average value of the stagnation temperatures on both sides of the mixing layer,

$$T_{0,ref} = \frac{1}{2}(T_{0,cool} + T_{0,\infty},).$$

Since the convective speed of the stagnation point, U_C, is known, we can use Eq. 8 to calculate the Mach number and the speed of sound at the stagnation point,

$$M_{ref} = \frac{U_C}{\sqrt{\gamma R T_{0,ref} - \frac{\gamma-1}{2}U_C^2}}, \tag{12}$$

$$a_{ref}^2 = \left(\frac{U_C}{M_{ref}}\right)^2 = \gamma R T_{0,ref} - \frac{\gamma-1}{2}U_C^2. \tag{13}$$

Due to the mixing nature, fluidic particles from both the low- and high-speed sides of the mixing layer will be combined at the stagnation point. Once the Mach number at the stagnation point is known, and assuming adiabatic process, the corresponding densities of the fluidic particles at the stagnation point can be calculated. Similar to the stagnation temperature, the reference density can be computed as the average of the local densities at the stagnation point,

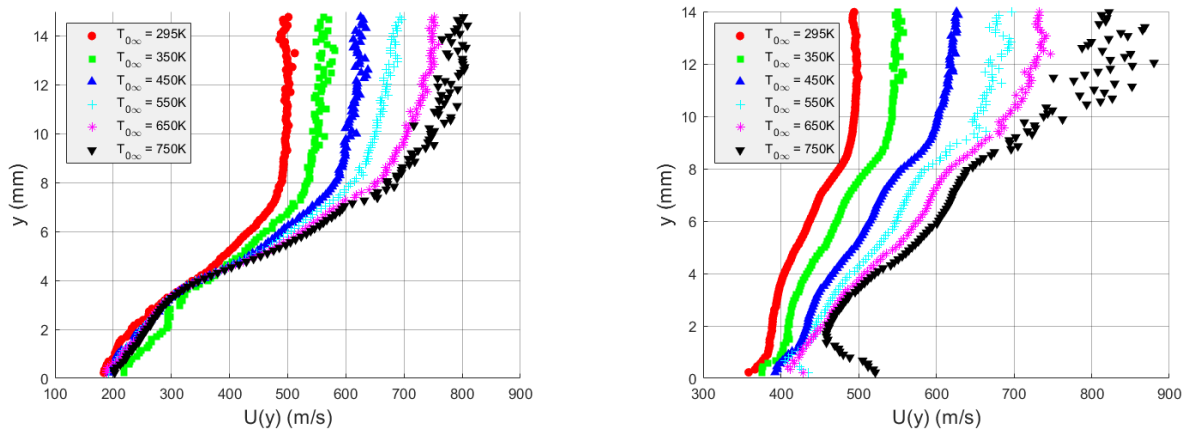

Fig. 17 Mixing layer velocity profiles for (a) air-air and (b) helium-air.

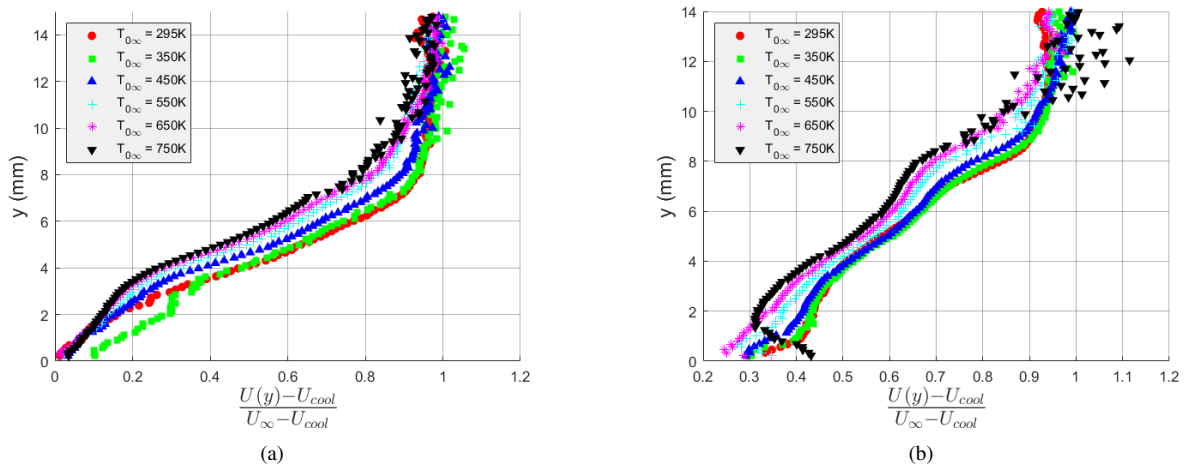

Fig. 18 Normalized mixing layer velocity profiles for (a) air-air and (b) helium-air.

$$\rho_{ref} = \frac{1}{2}\left[\rho_{cool}\left(\frac{1+\frac{\gamma-1}{2}M_{cool}^2}{1+\frac{\gamma-1}{2}M_{ref}^2}\right)^{\frac{1}{\gamma-1}} + \rho_\infty\left(\frac{1+\frac{\gamma-1}{2}M_\infty^2}{1+\frac{\gamma-1}{2}M_{ref}^2}\right)^{\frac{1}{\gamma-1}}\right]. \tag{14}$$

When the experimentally-measured values of OPD_{rms} are plotted against the new proposed model, Eq. 11 with reference quantities calculated using Eq. 13 and Eq. 14, the agreement, while still showing some scatter, is good, see Fig. 19(b).

2. Model: Helium-Air Case

The subsonic model, Eq. 3, was also tried for the helium-air case. The results are presented in Fig. 20(a). Clearly, the measured results do not show any linear dependence, since the subsonic model should not work for the case of mixing of dissimilar gases. In the air-air case, the densities across the mixing layer were similar, see Table 2, and the density fluctuations are mostly due to pressure variations inside vortical structures. In the helium-air case, density on the cooling (helium) side are significantly lower than the density in the freestream, see Table 3. So, it is reasonable to assume that the density fluctuations are mostly due to mixing of light gas (helium) and heavy gas (air). If we ignore

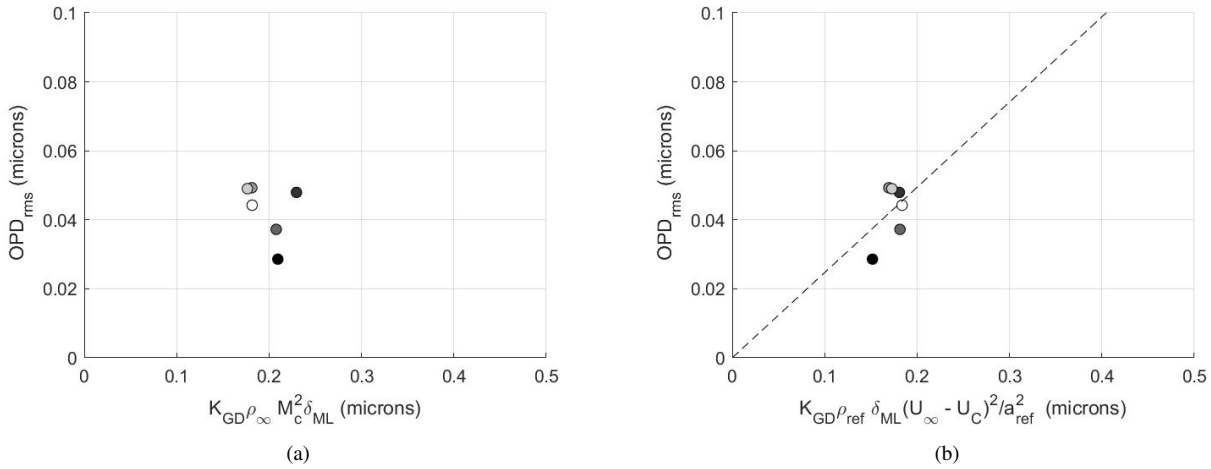

Fig. 19 OPD_{rms} **for the air-air case versus (a) subsonic scaling, Eq. 3 and (b) a new proposed pressure-driven scaling, Eq. 11. Darker symbols correspond to the lower stagnation temperatures, and lighter symbols correspond to higher stagnation temperatures.**

the pressure variations, the density variations will be due to velocity-dependent adiabatic cooling/heating. A similar mechanism is present in compressible turbulent boundary layers, allowing to develop useful aero-optical models [11, 13]. If pressure fluctuations are ignored, from the equation of state it follows that the density fluctuations are proportional to the temperature variations,

$$\frac{\rho_{rms}}{\rho_{ref}} = \frac{T_{rms}}{T_{ref}}.$$

In turn, a Strong Reynolds Analogy links the temperature and velocity fluctuations [11, 19],

$$C_P T_{rms} \sim U_{ref} u_{rms},$$

where U_{ref} is some reference speed. Combining the above equations, recognizing that for the mixing layers $u_{rms} \sim (U_\infty - U_{cool})$ [19], after some manipulations and using the same bulk-flow approach, we get the following equation for the level of aero-optical distortions in predominantly mixing flows,

$$OPD_{rms} \sim K_{GD}\rho_{rms}\Lambda \sim K_{GD}\rho_{ref}\frac{U_{ref}(U_\infty - U_{cool})}{a_{ref}^2}\Lambda. \tag{15}$$

For the reference speed, we can use the convective speed value, $U_{ref} = U_C$. Similar to the approach used in developing the pressure-dominant model for the air-air case, for the reference density and the square of the speed of of sound, we assume that they are a weighted linear combination of the corresponding quantities on both sides of the mixing layer,

$$\begin{aligned} \rho_{ref} &= \beta\rho_\infty + (1-\beta)\rho_{cool}, \\ a_{ref}^2 &= \beta a_\infty^2 + (1-\beta)a_{cool}^2 \end{aligned} \tag{16}$$

where β is weighting parameter. Since density fluctuations are proportional to the local density, most of the contribution to the density variations are expected to be from heavy density (air) side of the mixing layer. Thus, β-parameter should be close to 1. After trial-and-error, it was found that $\beta = 0.85$ resulted in a very good agreement with the proposed mixing-dominant model, as demonstrated in Fig. 20(b).

Both models rely on the convective speed, U_C, Eq. 9. This equation was derived under the assumption of the low convective Mach number limit [9]. For presented results, the convective Mach numbers were in the range of 0.55 and 0.85 for the air-air case and between 0.12 and 0.26 for the helium-air case. The convective Mach numbers for the air-air case might not considered to be low, possibly explaining the deviation of the air-air experimental data from the pressure-driven model in Fig. 19(b). So, the presented models should be considered as preliminary models for low

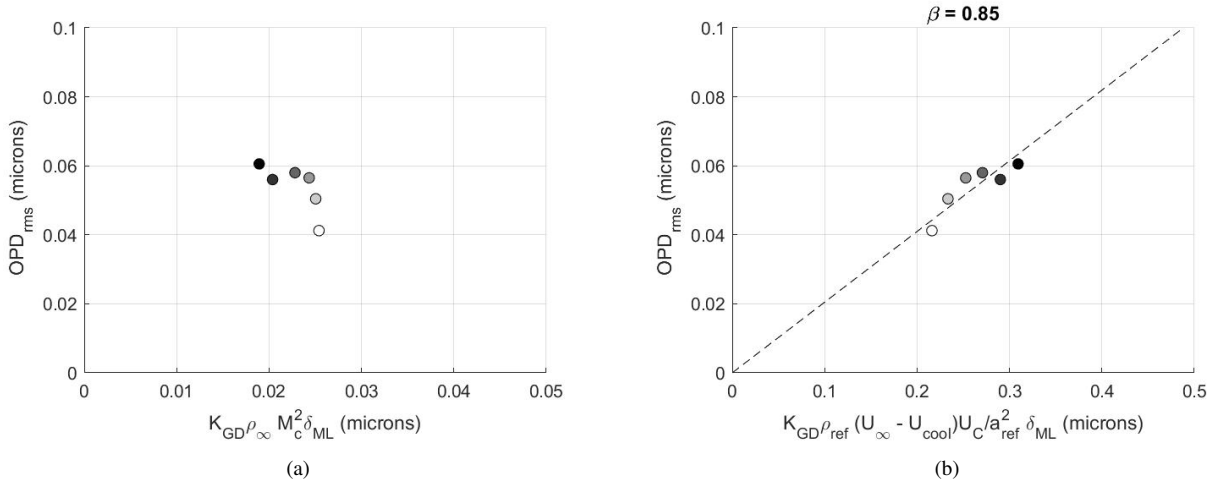

Fig. 20 OPD_{rms} for helium-air experiments versus (a) a subsonic model, Eq. 3 and (b) a new proposed mixing-dominant scaling, Eq. 15 with $\alpha = 0.85$. Darker symbols correspond to the lower stagnation temperatures, and lighter symbols correspond to higher stagnation temperatures.

supersonic speeds only. The presented models should be used with caution in case of high supersonic and hypersonic freestream speeds, as the difference between the freestream and the cooling jet speeds, and the related convective Mach numbers become large. Also, both models use the bulk-flow approach, which works for adiabatic wall boundary layers, but provided wrong predictions for boundary layers with non-adiabatic walls [13]. Future work will include the usage of the linking equation to develop the aero-optical models of the mixing layers, as this approach was demonstrated to develop a model which agreed much better with the experimental results for non-adiabatic wall boundary layers [13].

V. Conclusions

Optical measurements of a total temperature-mismatched supersonic mixing layer were made using time-resolved Shack-Hartmann WFS and Schlieren photography measurement techniques. The mixing layer was created by a two-dimensional jet blown through a backward-facing step with a depth of $5mm$. Using air as a test gas, the jet exit Mach number was $M \approx 0.53$. With helium as a test gas, the jet exit Mach number was $M \approx 0.30$. The jet was placed at the wall of a $M = 2$ wind tunnel and connected to an external gas supply to match the static pressure in the test section. Spanwise Schlieren measurements in the spanwise direction over an area with a diameter of 125 mm were made at sampling frequencies of 25 kHz and 100 kHz. Wall-normal Shack-Hartmann WFS measurements in the direction normal to the mixing layer with a beam diameter of 50 mm were performed, with the edge of the beam set 15 mm downstream of the cooling nozzle exit. Wind tunnel total temperature was varied between $295K$ and $750K$. To quantify the contaminating aero-optical effects of the opposite boundary layer, additional Shack-Hartmann WFS measurements were taken with the jet test section removed.

Flow parameters including jet exit velocity and mixing layer thickness were extracted from Schlieren measurements using optical velocity techniques. Time-averaged levels of aero-optical distortions, expressed as OPD_{rms} values, were extracted from Shack-Hartmann WFS data. Two new scaling models were proposed. For the air-air case, the model is based on optical distortions induced by pressure "wells" inside the coherent vortical structures spanned in the spanwise direction. For the helium-air case, a different model was developed, based on density fluctuations caused by the mixing of two gases with highly dissimilar densities. The proposed models provide a better agreement to the experimental data than the subsonic model developed for shear layers. The models can be used to predict aero-optical distortions caused by cooling flow over optical windows on supersonic vehicles.

Future work will include surface measurements of pressure and heat flux on the cavity wall to quantify the aero-thermal environment of the cooled window. In addition, other optical measurement techniques such as Planar Laser-Induced Fluorescence (PLIF) will be conducted to more accurately describe the mixing properties of the flow. Both models will be used to develop a unified model of optical distortions due to the compressible mixing layers. We also plan to perform the similar measurements at higher freestream Mach number. Such measurements will serve

to assist in the design of hypersonic optical windows such that the window is sufficiently cooled while minimizing aero-optical distortions.

Acknowledgements

This work is supported by the Office of Naval Research, Grant number N00014-22-1-2454 with Dr. Eric Marineau serving as program manager. The U.S. Government is authorized to reproduce and distribute reprints for governmental purposes notwithstanding any copyright notation thereon.

The authors also would like to thank Philip Lax for his help setting up the experiments and operating the tunnel. We also would like to thank Zareb Noel for his help in aligning the optical components.

References

[1] Juhany, K. A., Hunt, M. L., and Sivo, J. M., "Influence of injectant Mach number and temperature on supersonic film cooling," *Journal of Thermophysics and Heat Transfer*, Vol. 8, No. 1, 1994, pp. 59–67. https://doi.org/10.2514/3.501, URL https://doi.org/10.2514/3.501.

[2] Aupoix, B., Mignosi, A., Viala, S., Bouvier, F., and Gaillard, R., "Experimental and Numerical Study of Supersonic Film Cooling," *AIAA Journal*, Vol. 36, No. 6, 1998, pp. 915–923. https://doi.org/10.2514/2.495, URL https://doi.org/10.2514/2.495.

[3] Sahoo, N., Kulkarni, V., Saravanan, S., Jagadeesh, G., and Reddy, K. P. J., "Film cooling effectiveness on a large angle blunt cone flying at hypersonic speed," *Physics of Fluids*, Vol. 17, No. 3, 2005. https://doi.org/10.1063/1.1862261, URL https://doi.org/10.1063/1.1862261, 036102.

[4] Zhang, W., Ju, L., Fan, Z., Fan, W., and Chen, S., "Optical performance evaluation of an infrared system of a hypersonic vehicle in an aero-thermal environment," *Opt. Express*, Vol. 31, No. 16, 2023, pp. 26517–26534. https://doi.org/10.1364/OE.496783, URL https://opg.optica.org/oe/abstract.cfm?URI=oe-31-16-26517.

[5] Wang, M., Mani, A., and Gordeyev, S., "Physics and Computation of Aero-Optics," *Annual Review of Fluid Mechanics*, Vol. 44, No. 1, 2012, pp. 299–321. https://doi.org/10.1146/annurev-fluid-120710-101152, URL https://doi.org/10.1146/annurev-fluid-120710-101152.

[6] Gordeyev, S., Jumper, E., and Whiteley, M., *Aero-Optical Effects: Physics, Analysis and Mitigation*, Wiley Series in Pure and Applied Optics, Wiley, 2023. URL https://books.google.com/books?id=hqujEAAAQBAJ.

[7] Kalensky, M., Wells, J., and Gordeyev, S. V., "Image degradation due to different in-flight aero-optical environments," *Optical Engineering*, Vol. 59, No. 10, 2020, p. 104104. https://doi.org/10.1117/1.OE.59.10.104104, URL https://doi.org/10.1117/1.OE.59.10.104104.

[8] Fitzgerald, E. J., and Jumper, E. J., "The optical distortion mechanism in a nearly incompressible free shear layer," *Journal of Fluid Mechanics*, Vol. 512, 2004, pp. 153–189. https://doi.org/10.1017/S0022112004009553.

[9] Papamoschou, D., and Roshko, A., "The compressible turbulent shear layer: an experimental study," *Journal of Fluid Mechanics*, Vol. 197, 1988, pp. 453 – 477. https://doi.org/10.1017/S0022112088003325.

[10] Kemnetz, M. R., "Analysis of the aero-optical component of the jitter using the stitching method," , 2019.

[11] Gordeyev, S., Smith, A. E., Cress, J. A., and Jumper, E. J., "Experimental studies of aero-optical properties of subsonic turbulent boundary layers," *Journal of Fluid Mechanics*, Vol. 740, 2014, pp. 214–253. https://doi.org/10.1017/jfm.2013.658.

[12] Lynch, K., Miller, N., Guildenbecher, D., Butler, L., and Gordeyev, S., "Aero-Optical Measurements of a Mach 8 Boundary Layer," *AIAA Journal*, Vol. 61, No. 3, 2023, pp. 991–1001.

[13] Gordeyev, S., Cress, J. A., Smith, A., and Jumper, E. J., "Aero-optical measurements in a subsonic, turbulent boundary layer with non-adiabatic walls," *Physics of Fluids*, Vol. 27, No. 4, 2015, p. 045110. https://doi.org/10.1063/1.4919331, URL https://doi.org/10.1063/1.4919331.

[14] Fassler, A., Leonov, S., and Gordeyev, S., "Optical effects of a temperature-mismatched supersonic mixing layer," *Unconventional Imaging, Sensing, and Adaptive Optics 2023*, Vol. 12693, edited by J. J. Dolne, M. F. Spencer, and S. R. Bose-Pillai, International Society for Optics and Photonics, SPIE, 2023, p. 1269316. https://doi.org/10.1117/12.2677429, URL https://doi.org/10.1117/12.2677429.

[15] Castillo, P., Gross, A., Fassler, A., Leonov, S., and Gordeyev, S., "Wall-Modeled Large-Eddy Simulation of Supersonic Mixing Layer for Aero-Optical Distortion Analysis," *to be presented at SciTech 2024*, 2024.

[16] Andrews, P., Lax, P., Elliott, S., Firsov, A., and Leonov, S., "Flow Characterization at Heated Air Supersonic Facility SBR-50," *Fluids*, Vol. 7, No. 5, 2022. https://doi.org/10.3390/fluids7050168, URL https://www.mdpi.com/2311-5521/7/5/168.

[17] Sontag, J., and Gordeyev, S., "Optical Diagnostics of Spanwise-Uniform Flows," *AIAA Journal*, Vol. 60, No. 9, 2022, pp. 5031–5045. https://doi.org/10.2514/1.J061692, URL https://doi.org/10.2514/1.J061692.

[18] Southwell, W. H., "Wave-front estimation from wave-front slope measurements," *Journal of the Optical Society of America (1917-1983)*, Vol. 7, No. 8, 1980, p. 998.

[19] Smits, A., and Dussauge, J., *Turbulent Shear Layers in Supersonic Flow*, Springer New York, 2006. URL https://books.google.com/books?id=KtpFdcTEbQQC.

[20] Wyckham, C. M., and Smits, A. J., "Aero-Optic Distortion in Transonic and Hypersonic Turbulent Boundary Layers," *AIAA Journal*, Vol. 47, No. 9, 2009, pp. 2158–2168. https://doi.org/10.2514/1.41453, URL https://doi.org/10.2514/1.41453.